Transport and Communications Science Journal, Vol 77, Issue 09 (11/2026), 1170-1184

Transport and Communications Science Journal

COMPARATIVE FLEXURAL PERFORMANCE OF PRIMITIVE, DIAMOND, AND GYROID TPMS CONCRETE BEAMS

Tran Anh Tuan[1,2], Hoang Viet Hai[1,2], Nguyen Hoang Quan[1,3], Tran Thi Bich Thao[1,2], Tran Bao Viet[1,3]

[1]University of Transport and Communications, No 3 Cau Giay Street, Hanoi, Vietnam

[2]Research Group R2026-UTC-09, University of Transport and Communications, No 3 Cau Giay Street, Hanoi, Vietnam

[3]Research Group R2026-UTC-07, University of Transport and Communications, No 3 Cau Giay Street, Hanoi, Vietnam

ARTICLE INFO

TYPE: Research Article
Received: 13/08/2026
Revised: 02/11/2026
Accepted: 09/11/2026
Published online: 15/11/2026
https://doi.org/10.47869/tcsj.77.9.4

* *Corresponding author*
Email: hoangviethai@utc.edu.vn; Tel: 0902385538

Abstract. This study investigates the nonlinear flexural behaviour of Primitive, Diamond, and Gyroid triply periodic minimal surface (TPMS) concrete beams using the Concrete Damaged Plasticity model in Abaqus/Standard. All beams had identical external dimensions, C30/37 concrete properties, and a nominal solid volume fraction of 50%, allowing topology to remain the main variable. A combined geometric-resolution and mesh sensitivity study was conducted, and the R24 models were adopted as the common comparative reference. Structural performance was evaluated using peak load, secant stiffness, accumulated external work up to a common post-peak load threshold, mass-normalized accumulated work, normalized deformation index, and damage distributions. Primitive exhibited the highest secant stiffness (46.5 kN/mm) and peak load (5.12 kN) but showed localized damage, rapid post-peak load reduction, and the lowest accumulated work (0.93 J). Diamond achieved a slightly lower peak load (4.77 kN) while providing the highest accumulated work (1.85 J) and mass-normalized accumulated work (0.39 J/kg), indicating a favorable balance between strength and work accumulation under the adopted numerical assumptions. Gyroid showed the lowest peak load (3.56 kN) but the highest normalized deformation index (2.16). The results demonstrate a clear topology-dependent trade-off among stiffness, strength, accumulated work, and deformation capacity, and provide preliminary numerical insights for future experimental validation and investigation of load-bearing, permeable TPMS concrete structures.

Keywords: TPMS; concrete; flexural behaviour; Concrete Damaged Plasticity; accumulated external work; normalized deformation index; architected porous concrete.

2026 University of Transport and Communications

1. INTRODUCTION

Triply Periodic Minimal Surface (TPMS) structures have attracted increasing attention because of their high stiffness-to-weight ratio, continuous load-transfer paths, and favourable energy-absorption characteristics. Unlike conventional strut-based lattices, which may develop stress concentrations at discrete nodal intersections, TPMS architectures consist of smooth, continuously interconnected surfaces that can promote more distributed stress transfer. Their mechanical response is strongly governed by topology, relative density, unit-cell size, and loading direction. Maskery et al. [1] demonstrated that Primitive, Diamond, and Gyroid structures exhibit distinct deformation mechanisms; under the investigated conditions, Primitive showed a relative elastic modulus more than twice that of Gyroid and Diamond, whereas the latter two exhibited a stronger contribution from local bending deformation.

Most TPMS studies have traditionally focused on metallic and polymeric materials, while their application to quasi-brittle cementitious materials remains comparatively limited. Recent studies nevertheless demonstrate that TPMS geometries can be physically realized in concrete and can substantially influence structural behaviour. Righi et al. [2] fabricated and tested P. Schwarz, Gyroid, and hybrid concrete units and showed good correspondence between numerically predicted high-stress regions and experimentally observed cracking. Le et al. [3] further investigated sheet- and solid-based Primitive, Diamond, Gyroid, and I-WP architectures using UHPC and steel-UHPC interpenetrating-phase composites, demonstrating strong topology-dependent anisotropy and mechanical behaviour. Other studies have used TPMS as internal reinforcement or material interfaces. Nguyen-Van et al. [4] showed that 3D-printed Primitive scaffolds can modify crack development and flexural response in concrete beams, while more recent investigations have demonstrated that TPMS-Primitive networks can promote stress redistribution, crack deflection, confinement, and damage tolerance in multi-phase cementitious beams [5,6]. Experimental work on additively manufactured cementitious systems has also shown that TPMS-inspired infill and graded lattice architectures can influence crack propagation and flexural performance [7]. Collectively, these studies confirm the potential of geometric architecture to control the mechanical response of cementitious materials; however, they involve different materials, reinforcement concepts, density distributions, and loading conditions.

This issue becomes particularly important for concrete because its quasi-brittle behavior differs fundamentally from that of ductile polymers and metals. Under flexural loading, structural performance is governed not only by elastic stiffness and peak resistance but also by tensile crack initiation, stiffness degradation, damage localization, load redistribution, and post-peak deformation. Therefore, a topology that provides high initial stiffness does not necessarily confer superior post-cracking resistance or energy absorption. A nonlinear comparison under identical material, geometric, and loading conditions is required to isolate the influence of TPMS topology itself.

A broader motivation for this research is the development of structurally efficient permeable concrete. Conventional pervious concrete drains through a randomly interconnected pore network, but its hydraulic benefits come with a well-established strength-porosity trade-off. Typical pervious concrete requires relatively high interconnected porosity, and increasing pore volume generally reduces compressive, tensile, flexural, and fracture resistance [8,9]. TPMS offers an alternative concept based on architected porosity, in which the solid load-bearing skeleton and interconnected void channels can be geometrically controlled rather than formed randomly. Recent experiments by Nazir et al. [10] on 3D-printed Gyroid structures demonstrated the possibility of combining high mechanical resistance with continuous water infiltration pathways. Their polymer-based specimens achieved compressive strengths of approximately 36-37 MPa, flexural strengths of 4.74-4.87 MPa, and infiltration rates of 6.50-7.43 cm/s. These values cannot be directly transferred to concrete due to differences in constituent materials and failure mechanisms; however, the results clearly demonstrate the potential of TPMS geometry to control the strength-permeability trade-off through pore architecture. The same study also emphasizes that unit-cell size and wall thickness directly affect the balance between load-bearing capacity and permeability.

Despite these advances, direct comparative studies of monolithic Primitive, Diamond, and Gyroid concrete structures subjected to identical nonlinear flexural conditions remain limited. Existing investigations have commonly considered TPMS reinforcement, multi-material systems, compression-dominated behaviour, elastic characteristics, or individual TPMS topologies. Consequently, the relationship between topology, simulated tensile-damage evolution, post-peak load retention, normalized deformation, and accumulated external work in monolithic concrete TPMS beams has not yet been sufficiently clarified. Establishing these relationships is an important first step before the same geometries can be evaluated as multifunctional porous concrete systems combining structural and hydraulic requirements.

Accordingly, the present study conducts a controlled finite-element comparison of Primitive, Diamond, and Gyroid TPMS concrete beams subjected to displacement-controlled three-point bending. All models have identical external dimensions, C30/37 concrete properties, and a nominal solid volume fraction of 50%, allowing topology to remain the principal design variable. Tensile cracking, compressive damage, and stiffness degradation are represented using the Concrete Damaged Plasticity (CDP) model. Mechanical performance is evaluated using peak load, secant stiffness at peak K_{sec}, accumulated external work to an 80%-of-peak descending-load threshold U_{80}, mass-normalized accumulated work SEA_{80}, and normalized deformation index DI_{80}, together with tensile-damage, compressive-damage, and stress distributions.

The main objective is to clarify the stiffness-strength-normalized deformation-cumulative work trade-off among the three TPMS topologies and to identify the structural characteristics most relevant to flexural performance. More broadly, this work provides the mechanical basis for the future development of load-bearing permeable concrete with controlled TPMS pore networks, in which sufficient structural capacity and effective water drainage can ultimately be considered coupled design objectives. Hydraulic permeability is not directly evaluated in the present study; future work will therefore combine mechanical testing with permeability, pore-connectivity, clogging, and hydraulic-flow analyses to determine whether TPMS concrete can provide a more favourable mechanical-hydraulic balance than conventional randomly porous

concrete. The present findings are computational and do not establish measured permeability, manufacturing feasibility, aggregate compatibility, or durability. The methodological contribution is a controlled comparison rather than a new constitutive law or experimentally validated design recommendation.

2. THEORETICAL FRAMEWORK AND NUMERICAL MODELING

2.1. Mathematical Definition and Generation of TPMS Geometries

Triply Periodic Minimal Surfaces (TPMSs) are periodic cellular architectures that can be described using implicit mathematical functions repeated in three spatial directions. In the present study, the Primitive (P), Diamond (D), and Gyroid (G) topologies are generated in a solid/network TPMS configuration using a level-set approximation. The solid domain is defined as:

$$\Omega_s = \{(x, y, z) | F(x, y, z) \geq c\} \tag{1}$$

where $F(x, y, z)$ is the implicit TPMS function and c is the iso-value controlling the amount of solid material. Accordingly, the present models represent one continuous solid domain separated by the TPMS interface, rather than a sheet-based TPMS configuration.

For a cubic unit cell with characteristic length L, the normalized spatial coordinates are defined as:

$$X = \frac{2\pi x}{L}, \qquad Y = \frac{2\pi y}{L}, \qquad Z = \frac{2\pi z}{L} \tag{2}$$

where x, y, and z denote the Cartesian coordinates. The implicit functions adopted for the three investigated topologies are expressed as follows [1]:

Primitive
$$\cos(X) + \cos(Y) + \cos(Z) = C_p \tag{3}$$

Gyroid
$$\sin(X)\cos(Y) + \sin(Y)\cos(Z) + \sin(Z)\cos(X) = C_G \tag{4}$$

Diamond
$$\sin(X)\sin(Y)\sin(Z) + \sin(X)\cos(Y)\cos(Z) + \cos(X)\sin(Y)\cos(Z) + \cos(X)\cos(Y)\sin(Z) = C_D \tag{5}$$

The iso-value c directly controls the solid volume fraction V_f , and consequently the porosity of the generated structure. Because the objective of this study is to isolate the influence of topology, all three configurations are designed to contain the same amount of material. A numerical bisection algorithm is therefore employed to determine the value of c corresponding to a target solid volume fraction of $V_f(\%)$. Owing to the symmetry of the adopted implicit functions, the numerical procedure gives C_P, C_D, $C_G = 0.000$, corresponding to a solid volume fraction of approximately 50.00% for all three TPMS configurations within the adopted geometric discretization. Maintaining an identical solid volume fraction provides a consistent basis for comparing the mechanical response of the Primitive, Diamond, and Gyroid topologies without introducing differences associated with material quantity.

To evaluate the influence of geometric discretization on the numerical results, the TPMS surfaces are first generated at three spatial resolutions, denoted R12, R18, and R24. These levels

correspond to increasing surface-grid/voxel resolution during the geometry-generation stage, before the models are transferred to Abaqus for finite-element discretization. A higher resolution provides a more accurate representation of the curved TPMS boundaries but also increases the resulting geometric complexity and computational cost. These R-level labels describe successive geometric surface-reconstruction resolutions; they do not specify an Abaqus element edge length. The absolute surface-grid pitch and minimum solid-feature dimensions are not available in the reported numerical dataset, so they are not assigned assumed values here.

It should be emphasized that R12, R18, and R24 describe the resolution used to reconstruct the TPMS geometry and do not directly represent the finite element size in Abaqus. The combined influence of geometric resolution and the resulting finite-element discretization is therefore assessed separately in the sensitivity study presented in the subsequent section. Changing R alters both the reconstructed boundary and the resulting C3D4 discretization, and therefore does not isolate finite-element mesh-size effects at fixed geometry.

2.2. Finite Element Model and Boundary Conditions

A nonlinear static analysis was performed in Abaqus using the implicit solver and Newton-Raphson iteration. Automatic incrementation was adopted with a minimum increment size of 10^{-7} to improve convergence during cracking and stiffness degradation.

Because of the complex curved TPMS geometry, all beams were discretized using four-node linear tetrahedral elements (C3D4). Each specimen had dimensions of 100×100×400 mm and contained 4×1×1 units cells with a nominal porosity of 50%. The beam longitudinal, vertical, and transverse directions were aligned with the Z-, Y-, and X-axes, respectively. For this 4 × 1 × 1 arrangement, the nominal repeat length is 100 mm in each coordinate direction; a study varying unit-cell number or loading orientation was not performed.

A three-point bending configuration with a 300 mm support span was adopted. The supports were centered at Z=50 and 350 mm and represented by 16-mm-wide nodal strips to avoid local stress singularities. At the left support, $U_x = U_y = U_z = 0$, while at the right support, $U_x = U_y = 0$ and U_z remained free, providing an approximate pin-roller condition. The prescribed nodal constraints approximate, but do not reproduce, frictionless experimental pin-roller contact. Constraining multiple nodes within each support strip may introduce local restraint and affect the computed stiffness and reaction distribution; this influence was not quantified in a separate support-sensitivity model.

Loading was applied under displacement control through a 16-mm-wide nodal strip at midspan (Z=200 mm). A downward displacement in the Y-direction was prescribed to approximate a distributed loading region without explicitly modelling rigid rollers and surface contact. The loading-strip nodes receive the prescribed displacement directly rather than force through a contact roller. No alternative roller-contact or support-strip-width analysis is available, and its influence must not be assumed negligible.

The load-deflection response was obtained from the total vertical reaction force RF2 at the supports and the midspan vertical displacement U2. These data were subsequently used to evaluate peak load, peak-load secant stiffness, normalized deformation, and cumulative external work.

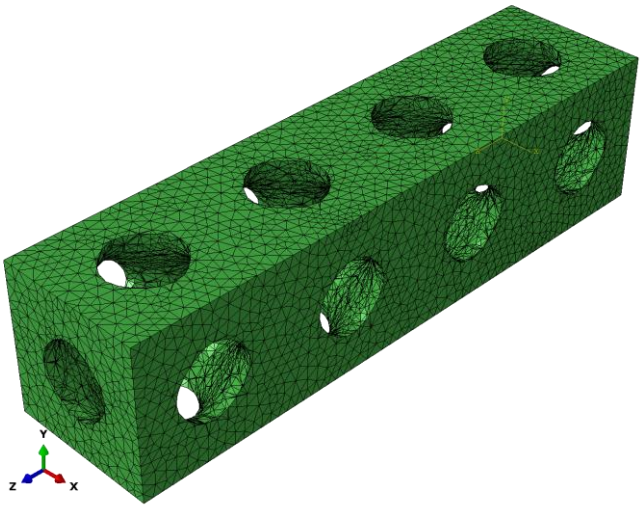


Figure 1. Representative 3D geometry of the Primitive TPMS beam at 50% porosity.

3. CONCRETE DAMAGED PLASTICITY MODEL

3.1. CDP Formulation

The Concrete Damaged Plasticity (CDP) model [11,12] was adopted to represent the nonlinear behaviour of concrete, including tensile cracking, compressive crushing, plastic deformation, and stiffness degradation. The model combines isotropic damage with plasticity and introduces two independent damage variables, d_t and d_c, for tension and compression, respectively. The corresponding degraded elastic stiffness may be expressed conceptually as:

$$E_t = (1 - d_t)E_0, \qquad E_c = (1 - d_c)E_0 \tag{6}$$

Where: E_0 is the initial elastic modulus. The CDP yield surface is pressure-dependent, allowing different failure responses under tensile and compressive stress states and representing the increased compressive resistance of concrete under multiaxial confinement.

3.2. Mesh Sensitivity and Fracture-Energy Considerations

Strain-softening models for quasi-brittle materials may exhibit mesh-dependent post-peak responses, because strain localization tends to occur within increasingly narrow regions as the mesh is refined. Fracture-energy-based regularization, commonly associated with the fictitious crack concept proposed by Hillerborg et al. [13], can reduce this dependency by relating the softening response to a characteristic element length.

In the present model, however, tensile softening is defined using a stress-cracking strain relationship rather than an explicit fracture-energy (G_f) regularization scheme. Consequently, some mesh sensitivity remains in the post-cracking response. A dedicated resolution and mesh-sensitivity study was therefore conducted to establish a consistent reference discretization for comparing the three TPMS configurations. No fixed-geometry mesh-refinement series, fracture-energy-based sensitivity study, or independently validated numerical benchmark was carried out. Accordingly, the post-peak indices should be regarded as comparative outputs of the specified CDP formulation, not mesh-objective predictions of fracture dissipation [14].

3.3. Material Properties and CDP Parameters

Concrete grade C30/37 was modeled in accordance with Eurocode 2 [15]. A density of ρ=2400 kg/m³ was assumed. For a 100×100×400 mm beam with a 50% solid volume fraction, the corresponding structural mass is approximately 4.8 kg. The elastic and strength properties were defined as: E_{cm}= 32.8 GPa, υ=0.20, f_{cm} = 38 MPa, f_{ctm} = 2.9 MPa.

The nonlinear compressive and tensile stress-strain relations and the corresponding damage variables were converted into discrete input data for Abaqus. The adopted CDP parameters were: dilation angle =36^0, eccentricity =0.1, f_{bo}/f_{co}, K=0.6667, and viscosity parameter =1.0×10^{-4}. These parameters define the shape and flow characteristics of the CDP yield surface, while the small-viscosity parameter was introduced to improve numerical convergence under severe stiffness degradation.

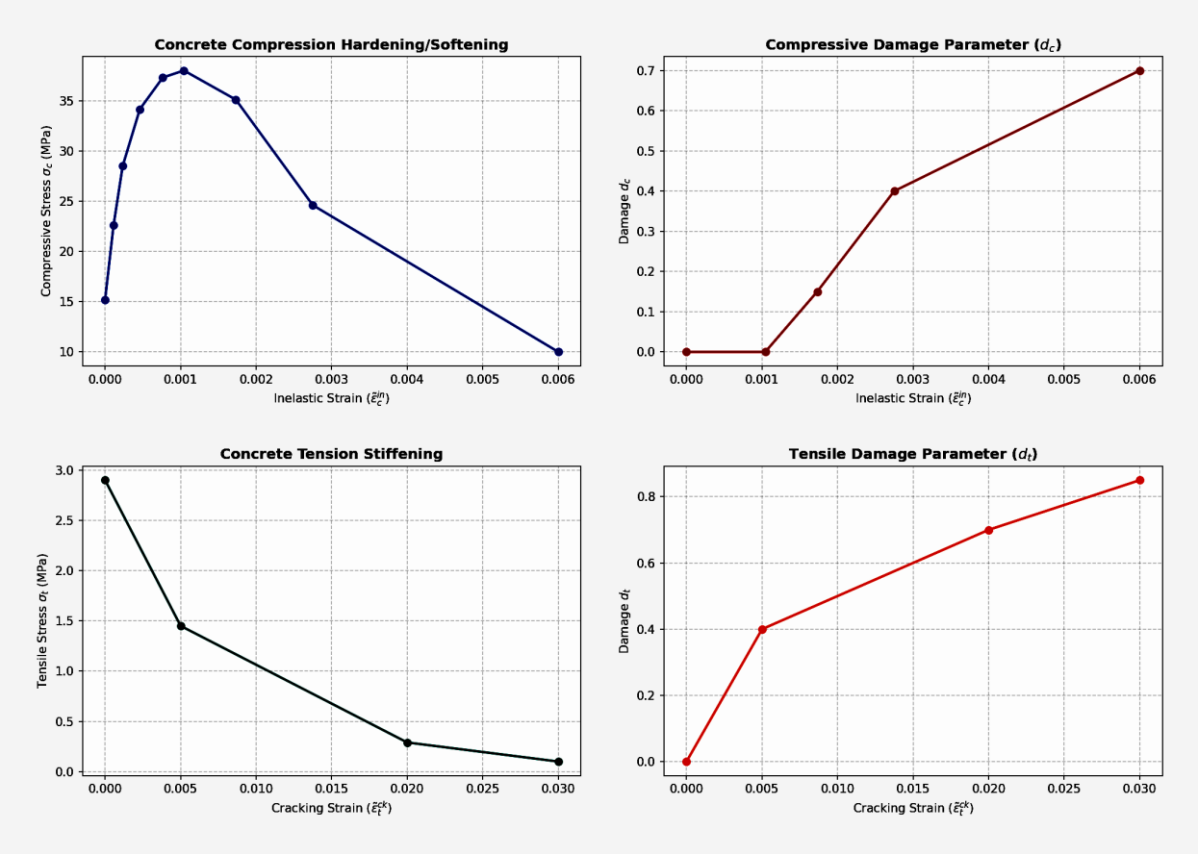


Figure 2. Stress-strain relationships and damage parameters adopted for C30/37 concrete.

4. RESULTS AND DISCUSSION

4.1. Load-displacement response

Figure 3 compares the load-displacement ($P-\delta$) responses of the Primitive, Diamond, and Gyroid beams at R24. All three curves exhibit three typical stages: an initial nearly linear response, a nonlinear pre-peak stage associated with progressive cracking, and a post-peak softening stage.

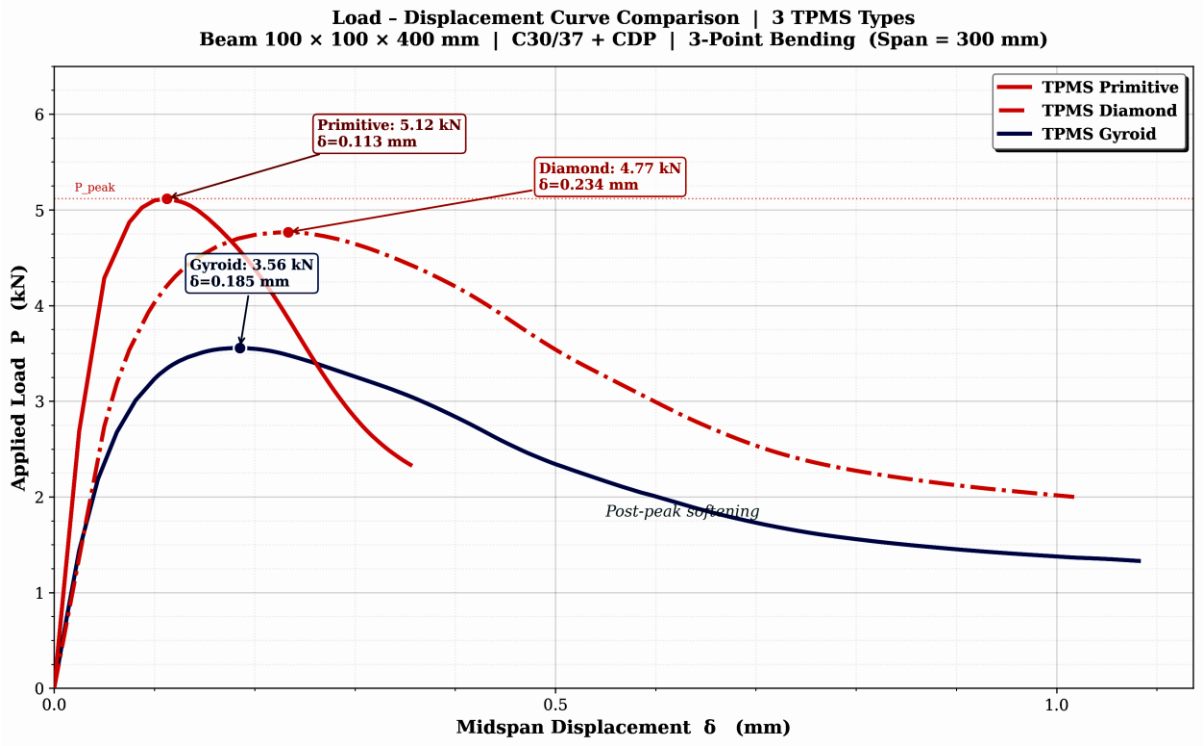


Figure 3. Load-displacement curves of the three TPMS beams at the R24 reference resolution.

The Primitive beam reaches the highest peak load, P_{peak} = 5.12 kN, and exhibits the steepest initial response. However, the load decreases rapidly after the peak, indicating relatively brittle failure. The Diamond beam reaches a slightly lower peak load of 4.77 kN but maintains a higher load over a larger post-peak displacement range, indicating a more gradual loss of load-carrying capacity. The Gyroid beam shows the lowest peak load, 3.56 kN, but retains a relatively extended post-peak deformation response at reduced load levels.

These differences are primarily associated with the internal load-transfer mechanisms of the three topologies. Primitive provides relatively direct load paths, thereby providing high flexural stiffness and strength, but damage tends to localize rapidly. Diamond promotes more distributed load transfer through its interconnected inclined regions, resulting in a more progressive post-peak response. Gyroid provides a smooth, continuous geometry, but local thin sections become damaged relatively early, reducing peak resistance and allowing damage to spread over a wider region. These are interpretations of the simulated stress and damage fields and are not experimentally verified crack mechanisms.

4.2. Geometric Resolution and Mesh Sensitivity

The resolution parameter R influences both the accuracy of the reconstructed TPMS surface and the resulting finite element discretization. Therefore, variations between R12, R18, and R24 should be interpreted as a combined geometric-resolution and mesh effect, rather than a conventional mesh-convergence study based solely on element size. This analysis cannot be described as an independent fixed-geometry finite-element mesh-convergence study.

Because four-node linear tetrahedral elements (C3D4) may produce an overly stiff bending response when the discretization is coarse, three resolution levels were examined to assess the stability of the predicted peak load.

Table 1. Comparative flexural-response metrics.

Topology	Resolution	Number of elements	Peak load (kN)	Solution time
Primitive	R12	62,541	5.33	17 min
Primitive	R18	206,007	5.22	35 min
Primitive	R24	449,482	5.12	125 min
Diamond	R12	77,255	5.10	20 min
Diamond	R18	213,783	4.90	85 min
Diamond	R24	455,839	4.77	219 min
Gyroid	R12	68,890	4.12	14 min
Gyroid	R18	197,631	3.62	78 min
Gyroid	R24	424,509	3.56	218 min

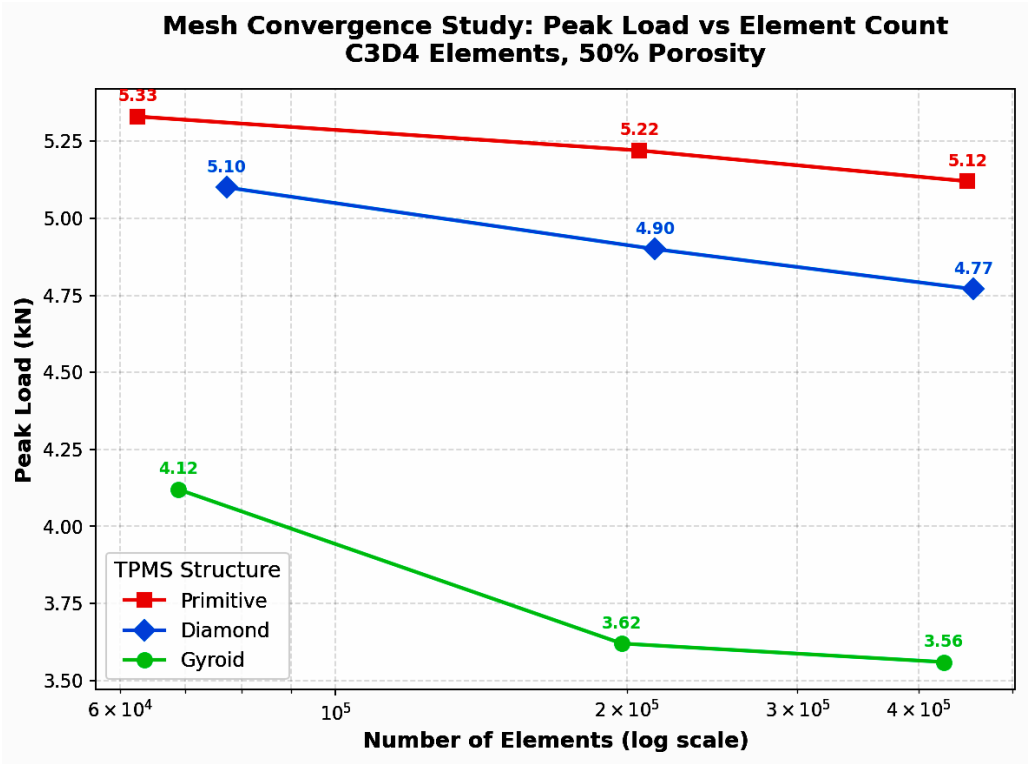


Figure 4. Sensitivity of peak load to geometric resolution and element count.

The predicted peak load decreases as geometric reconstruction resolution and the accompanying FE discretization are refined. From R12 to R24, the reduction is approximately 4% for Primitive, 6% for Diamond, and 14% for Gyroid. The larger change observed for Gyroid indicates that its curved, locally thin geometry is more sensitive to the adopted surface resolution.

Resolution dependence of the reported indices was further assessed by comparing U_{80} and DI_{80} between R18 and R24.

Table 2. Resolution sensitivity of peak load and post-peak performance indicators.

Topology	Resolution	Peak load (kN)	U_{80} (J)	DI_{80}
Primitive	R18	5.22	0.95	1.94
Primitive	R24	5.12	0.93	1.96
Diamond	R18	4.90	1.90	1.94
Diamond	R24	4.77	1.85	1.97
Gyroid	R18	3.62	1.28	2.14
Gyroid	R24	3.56	1.21	2.16

Between R18 and R24, the post-peak indices vary by less than approximately 6%. Gyroid shows the largest change in U_{80}, whereas DI_{80} remains relatively stable for all three topologies. R24 was therefore adopted as the finest available common comparison level, without claiming independent mesh convergence. From R18 to R24, U_{80} changed by 2.1% (Primitive), 2.6% (Diamond), and 5.5% (Gyroid), while DI_{80} changed by approximately 1.0%, 1.5%, and 0.9%, respectively. These changes cannot be extrapolated to meshes finer than R24 or to fracture-energy-regularized models.

Some discretization sensitivity remains because tensile softening in the present CDP model is defined using a stress-cracking strain relationship without fracture-energy regularization. R24 was selected as the common reference for the reported comparisons, while acknowledging the absence of an element-size-only convergence analysis. The reported solution times are provided only as a relative indication of computational cost, as they depend on the hardware and solver configuration.

4.3. Damage and Stress Distributions

Damage and stress contours obtained from the R24 simulations are compared to investigate the failure mechanisms of the three TPMS topologies. To ensure consistent visual comparison, identical contour ranges were used for all models. Results were extracted at 50% and at the final converged state. An equal fraction of the analysis step time need not represent the same physical loading stage across different topologies; neither panel is explicitly synchronized at each individual P_{peak} nor at the descending-branch 0.8Ppeak point. The presented DAMAGET-type fields represent modelled tensile damage, not measured crack opening.

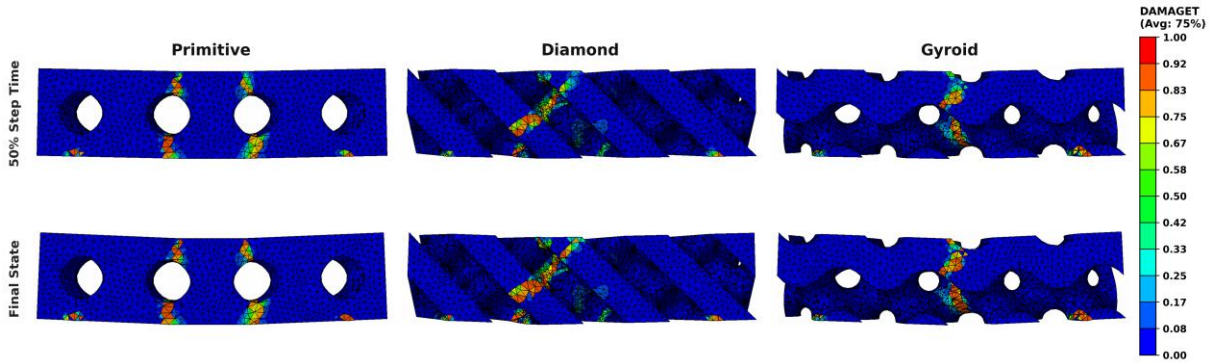


Figure 5. Simulated tensile-damage distributions at 50% step time and the final converged state.

The simulated tensile-damage distributions differ among the three topologies. In the Primitive beam, tensile damage becomes strongly localized near the midspan and develops into

a relatively narrow damage band. This localized failure is consistent with the rapid post-peak load reduction observed in the $P-\delta$ curve. For the Diamond beam, damage develops across multiple inclined, interconnected regions rather than concentrating immediately within a single vertical band. This more distributed damage pattern promotes progressive stress redistribution and is consistent with its higher modeled post-peak load retention and accumulated external work U_{80}. In the Gyroid beam, local damage initiates relatively early in geometrically thin regions of the continuous curved network. Although this reduces the peak load, damage subsequently spreads over a broader portion of the structure. This distributed degradation is consistent with the comparatively large DI_{80} obtained for the Gyroid topology. Among the numerical snapshots compared, the contour results suggest that TPMS topology affects not only peak resistance but also damage localization, stress redistribution, and post-peak deformation. Primitive favours stiffness and strength but develops more localized failure, Diamond provides the most balanced redistribution mechanism, while Gyroid exhibits lower peak resistance but more spatially distributed damage. Because the two snapshots are not matched to Ppeak and the 80% descending-load state separately for each topology, they are used only for qualitative spatial comparison; no explicit crack-opening measurement is claimed.

4.4. Quantitative Comparison of Stiffness, Accumulated External Work, and Normalized Deformation

To ensure a consistent comparison and minimize discretization-related bias, all quantitative results in this section were obtained from the R24 reference models. The nominal target solid volume fraction was V_f= 50.00% for all three topologies, corresponding to an idealized solid volume of 2.000×106 mm³ and a structural mass of M=4.80 kg. The reported 4.80 kg mass is calculated from this nominal volume and the assumed density of 2400 kg/m³; it is not a verification of the element-integrated meshed volume or minimum ligament size.

The mechanical indices were calculated from the load-displacement curves as follows:

$$K_{sec} = \frac{P_{peak}}{\delta_{peak}} \tag{7}$$

Where: K_{sec} is the secant stiffness at peak load. Specifically, $K_{sec} = P_{peak}/\delta_{peak}$; it is a peak-load secant stiffness, not the initial tangent stiffness.

$$U_{80} = \int_0^{\delta_{80}} P(\delta)d(\delta) \tag{8}$$

where δ_{80} is the post-peak displacement at which the load decreases to 0.8 times its peak value.P_{peak} This common, normalized post-peak criterion allows accumulated external work to be compared consistently. Because Equation (8) integrates P(δ) from $\delta = 0$ to δ_{80}, U_{80} includes work before and after the peak. It is the total applied external work up to δ_{80}, not exclusively the post-peak work, and not a direct measure of dissipated fracture energy. A post-peak-only area would require integration from δpeak to δ_{80} and is not reported here.

The mass-normalized accumulated work and the normalized deformation index are defined as follows. Here, $DI_{80} = \delta_{80}/\delta_{peak}$, where δ_{80} is the displacement at peak load and δ_{peak} is the peak displacement. Since no yield displacement was defined, DI_{80} must not be interpreted as the conventional structural ductility ratio.

$$SEA_{80} = \frac{U_{80}}{M}, \quad DI_{80} = \frac{\delta_{80}}{\delta_{peak}} \tag{9}$$

When load is expressed in kN and displacement in mm, the area under the load-displacement curve is directly obtained in joules because 1kN·mm=1J.

Table 3. Comparison of peak load, stiffness, accumulated external work, and normalized deformation indicators at R24 resolution.

Topology	P_{peak} (kN)	δ_{peak} (mm)	δ_{80} (mm)	K_{sec} (kN/mm)	U_{80} (J)	DI_{80}	SEA_{80} (J/kg)
Primitive	5.12	0.110	0.215	46.5	0.93	1.96	0.19
Diamond	4.77	0.230	0.453	20.7	1.85	1.97	0.39
Gyroid	3.56	0.190	0.410	18.7	1.21	2.16	0.25

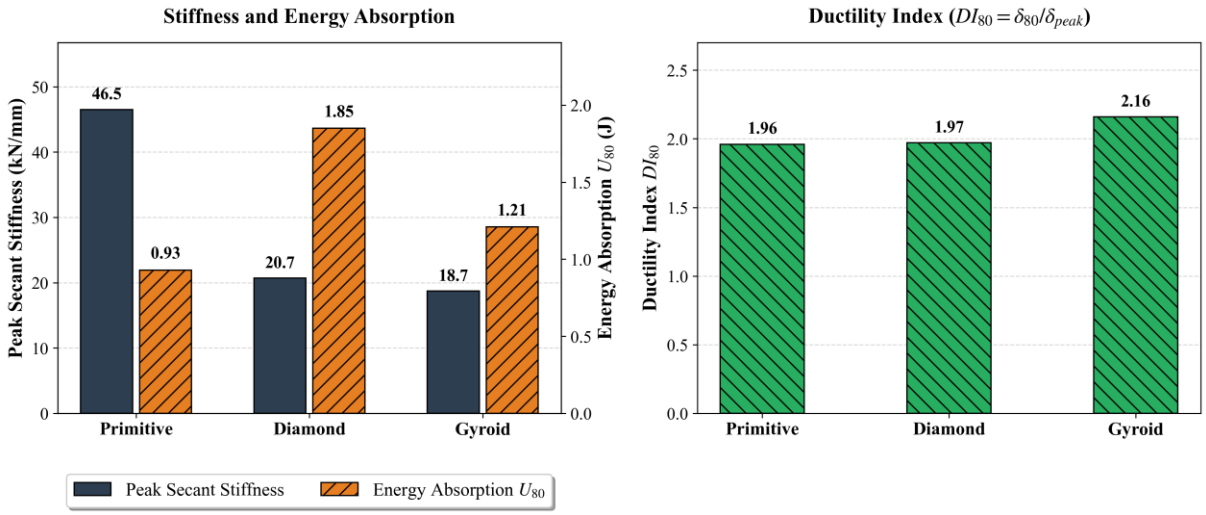


Figure 6. Comparison of the mechanical performance indices obtained from the R24 models. The plotted U_{80} bars represent the cumulative external work to δ_{80}, and DI_{80} denotes $\delta_{80}/\delta_{peak}$; these definitions govern the interpretation of the indices plotted.

Primitive provides the highest stiffness and load-carrying capacity. Its K_{sec} of 46.5 kN/mm is more than twice that of Diamond and Gyroid, while its peak load reaches 5.12 kN. However, its relatively low U_{80}= 0.93 J indicates the smallest cumulative external work to the defined descending-load threshold among the three numerical cases.

Diamond shows the largest U_{80} among the three simulated topologies, while retaining a peak load close to Primitive. Although its peak load of 4.77 kN is slightly lower than that of Primitive, it achieves the highest U_{80} = 1.85 J and SEA_{80} = 0.39 J/kg. This result is consistent with the more distributed damage pattern observed in Section 4.3 and indicates a more sustained simulated load-displacement response along the selected integration interval.

Gyroid has the lowest peak load and stiffness but the highest normalized deformation index, DI_{80}=2.16. This indicates that the structure can reach a larger normalized post-peak displacement before its load decreases to 80% of the peak value. However, a high DI_{80} should not be interpreted independently as superior structural performance because the Gyroid also carries a substantially lower load than the other two topologies.

The present ranking in peak resistance, Primitive > Diamond > Gyroid, is qualitatively consistent with the topology-dependent trends reported by Maskery et al [1] for additively

manufactured polymer TPMS structures. However, direct quantitative comparison is not appropriate because the material system and loading conditions are different. In polymer TPMS structures, substantial plastic deformation can produce an extended stress plateau, whereas the present concrete models exhibit pronounced post-peak softening associated with quasi-brittle cracking.

Previous studies on metallic TPMS structures [16,17] have also reported that sheet-based TPMS configurations can provide greater specific energy absorption than solid/network configurations because of their shell-dominated deformation mechanisms. The much lower SEA_{80} values obtained here, ranging from 0.19 to 0.39 J/kg, are expected for quasi-brittle concrete and should therefore not be directly compared with the much higher energy-absorption values commonly reported for ductile metallic TPMS structures. However, the U_{80}/m metric used here is cumulative external work to a specified 80%-of-peak descending-load state; differences in integration bounds, constitutive response, and material system prevent direct interpretation as the same energy-dissipation measure used in metallic TPMS studies.

The results reveal a clear topology-dependent trade-off. Primitive is dominated by stiffness and peak resistance, Diamond provides the highest U_{80} accumulated external work, and Gyroid provides the largest normalized post-peak deformation capacity**.** These differences confirm that selecting a TPMS topology should depend on the required structural function rather than on a single performance indicator.

5. CONCLUSIONS

This study compared the nonlinear flexural behavior of Primitive, Diamond, and Gyroid concrete TPMS beams under identical material, geometric, and loading conditions. The main conclusions are as follows:

- Primitive exhibited the highest secant stiffness (K_{sec} = 46.5 kN/mm) and peak load (P_{peak}= 5.12 kN), indicating the greatest flexural rigidity and load-carrying capacity. However, its strongly localized damage resulted in a rapid numerical post-peak softening and the lowest cumulative external work U_{80} (U_{80} = 0.93 J).
- Diamond provided the highest cumulative external work among the simulated cases under the specified modeling assumptions. It reached a peak load of 4.77 kN and achieved the highest U_{80} (U_{80} =1.85 J) and mass-normalized accumulated work (SEA_{80}= 0.39 J/kg). Its more distributed damage pattern contributed to improved post-cracking load retention.
- Gyroid showed the highest normalized deformation index (DI_{80} = 2.16), indicating the largest normalized post-peak deformation capacity. However, it had the lowest stiffness and peak load (P_{peak} = 3.56 kN), mainly due to early damage in locally thin regions of the curved network.

The results indicate a topology-dependent trade-off within the present computational scope: Primitive favors stiffness and strength, Diamond provides the highest U80 cumulative external work, while Gyroid offers greater post-peak deformation capacity.

The present findings should be interpreted within the limitations of the numerical model. The 4×1×1 unit-cell configuration may be affected by size and boundary effects, whereas using nodal strips instead of explicit roller contact may locally increase support stiffness. In addition,

the CDP tensile softening law was defined using cracking strain without fracture-energy regularization, so some mesh sensitivity remains in the post-peak response. Experimental three-point bending tests are therefore required to validate the predicted load-displacement behavior and damage mechanisms. Future work should also investigate unit-cell size, porosity, fracture-energy regularization, and hydraulic permeability to support the development of load-bearing and permeable TPMS concrete structures. The work index U_{80} includes pre-peak and post-peak work, while DI_{80} is a displacement ratio without a yield-point definition. The R12-R24 comparison jointly changes surface resolution and element discretization and therefore does not establish mesh-objective post-peak behavior. Figure 5 shows tensile-damage distributions at step-based, rather than mechanically matched, load states.

The 50% solid fraction, single 4 × 1 × 1 cell arrangement, and one loading orientation also limit generalization. No independent experimental/validated numerical benchmark, solid concrete control beam, actual mesh volume and minimum-feature audit, or roller-contact sensitivity study was included. For future physical realization, the minimum ligament dimensions must be checked against aggregate size and feasible manufacturing routes (e.g., fine-aggregate printing or removable-formwork casting); permeability, clogging, and durability require separate testing. These unresolved issues are acknowledged as limitations rather than inferred favorable results.

ACKNOWLEDGMENTS

This research is funded by the University of Transport and Communications (UTC) under grant number T2026-CT-004TD

REFERENCES

[1]. I. Maskery, L. Sturm, A. O. Aremu, A. Panesar, C. B. Williams, C. J. Tuck, R. D. Wildman, I. A. Ashcroft, R. J. M. Hague, Insights into the mechanical properties of several triply periodic minimal surface lattice structures made by polymer additive manufacturing, Polymer, 152 (2018) 62-71. https://doi.org/10.1016/j.polymer.2017.11.049

[2]. M. Righi, F. Yavartanoo, S. Alaeva, D. Bolhassani, Design, fabrication and analysis of triply periodic minimal surface concrete units, Journal of Building Engineering, 98 (2024) 111286. https://doi.org/10.1016/j.jobe.2024.111286

[3]. B.-A. Le, B.-V. Tran, T.-S. Vu, Q.-B. Nguyen, H.-Q. Nguyen, X. Chateau, Anisotropy and mechanical characteristics of ultra-high performance concrete and its interpenetrating phase composite with triply periodic minimal surface architectures, Journal of Applied Mechanics, 91(9) (2024) 091008. https://doi.org/10.1115/1.4065901

[4]. V. Nguyen-Van, N. K. Choudhry, B. Panda, H. Nguyen-Xuan, P. Tran, Performance of concrete beam reinforced with 3D printed bioinspired Primitive scaffold subjected to three-point bending, Automation in Construction, 134 (2022) 104060. https://doi.org/10.1016/j.autcon.2021.104060

[5]. V. Nguyen-Van, S. Sankeeth, N. Das, Z. Li, J. Lao, S. Qian, Low-carbon cementitious composite beams incorporating plastic TPMS-Primitive reinforcement and sludge-derived biochar: Mechanical performance, durability, and sustainability, Journal of Building Engineering, 128 (2026) 116630. https://doi.org/10.1016/j.jobe.2026.116630

[6]. V. Nguyen-Van, C. J. Cheah, T. Ngo, Y. M. Xie, N. S. Ha, Multi-material design strategy for low-carbon cementitious composite structures based on bio-inspired geometries, Structures, 87 (2026) 111733.https://doi.org/10.1016/j.istruc.2026.111733

[7]. B. Zhang, W. De Corte, T. Ooms, R. Wan-Wendner, Mechanical properties of particle-bed 3D printed concrete infill patterns, Additive Manufacturing, 106 (2025) 104803. https://doi.org/10.1016/j.addma.2025.104803

[8]. A. K. Chandrappa, K. P. Biligiri, Pervious concrete as a sustainable pavement material-Research findings and future prospects: A state-of-the-art review, Construction and Building Materials, 111 (2016) 262-274. https://doi.org/10.1016/j.conbuildmat.2016.02.054

[9]. F. Yu, J. Guo, J. Liu, H. Cai, Y. Huang, A review of the pore structure of pervious concrete: Analyzing method, characterization parameters and the effect on performance, Construction and Building Materials, 365 (2023) 129971. https://doi.org/10.1016/j.conbuildmat.2022.129971

[10]. U. Nazir, M.-C. Liao, A. Nazir, J. J. Ekaputri, A. I. Farah, High strength and highly permeable 3D-printed plastic gyroid TPMS structures for pervious pavement applications, International Journal of Pavement Engineering, 27(1) (2026) 2649909. https://doi.org/10.1080/10298436.2026.2649909

[11]. J. Lubliner, J. Oliver, S. Oller, E. Oñate, A plastic-damage model for concrete, International Journal of Solids and Structures, 25(3) (1989) 299-326. https://doi.org/10.1016/0020-7683(89)90050-4

[12]. J. Lee, G. L. Fenves, Plastic-damage model for cyclic loading of concrete structures, Journal of Engineering Mechanics, 124(8) (1998) 892-900. https://doi.org/10.1061/(ASCE)0733-9399(1998)124:8(892)

[13]. A. Hillerborg, M. Modéer, P.-E. Petersson, Analysis of crack formation and crack growth in concrete by means of fracture mechanics and finite elements, Cement and Concrete Research, 6(6) (1976) 773-781. https://doi.org/10.1016/0008-8846(76)90007-7

[14]. Dassault Systèmes SIMULIA, Abaqus 2024 Documentation: Concrete Damaged Plasticity, Dassault Systèmes, 2024.

[15]. CEN, EN 1992-1-1:2004, Eurocode 2: Design of Concrete Structures-Part 1-1: General Rules and Rules for Buildings, European Committee for Standardization, Brussels, Belgium, 2004.

[16]. O. Al-Ketan, R. K. Abu Al-Rub, Multifunctional mechanical metamaterials based on triply periodic minimal surface lattices, Advanced Engineering Materials, 21(10) (2019) 1900524. https://doi.org/10.1002/adem.201900524

[17]. D. W. Abueidda, M. Elhebeary, C.-S. Shiang, S. Pang, R. K. Abu Al-Rub, I. M. Jasiuk, Mechanical properties of 3D printed polymeric Gyroid cellular structures: Experimental and finite element study, Materials & Design, 165 (2019) 107597. https://doi.org/10.1016/j.matdes.2019.107597